SEECCM III
3rd South-East European Conference on Computational Mechanics-
an ECCOMAS and IACM Special Interest Conference
M. Papadrakakis, M. Kojic, I. Tuncer, V. Papadopoulos (eds.)
Kos Island, Greece, 12–14 June 2013

IMPROVING THE ACCURACY OF A FINITE-VOLUME METHOD FOR COMPUTING RADIATIVE HEAT TRANSFER IN THREE-DIMENSIONAL UNSTRUCTURED MESHES

Georgios N. Lygidakis[1] and Ioannis K. Nikolos[2]

[1,2] Department of Production Engineering and Management, Technical University of Crete
Chania, GR-73100, Greece
[1]e-mail: glygidakis@isc.tuc.gr
[2] e-mail: jnikolo@dpem.tuc.gr

Keywords: Radiative heat transfer, node-centered finite-volume method, 2nd order accurate spatial/temporal scheme, h-refinement.

Abstract. *In recent years, the Finite-Volume Method (FVM), being one of the most widely applied techniques in Computational Fluid Dynamics (CFD), has gained some popularity in solving radiative heat transfer problems. In order to avoid excessive amounts of false scattering and improve the accuracy of this method, two techniques, well established in CFD scientific field, were developed for a parallelized algorithm using FVM for the prediction of radiative heat transfer for absorbing, emitting and scattering gray media in hybrid unstructured grids. The first one considers a second order accurate spatial/temporal scheme for the calculation of radiative heat fluxes, while the second one uses a grid adaptation technique during the progress of the solution. The second order spatial scheme is based on the Monotonic Upstream Scheme for Conservation Laws (MUSCL) reconstruction of the radiative intensities, using additionally a slope limiter to control the total variation of the reconstructed field. A second order in time Runge-Kutta method is utilized for the solution of the time dependent Radiative Transfer Equation (RTE), avoiding the oscillations derived from the coupling of the higher order spatial scheme and the standard iterative solution of the non time-dependent RTE. The second technique is the h-refinement, which enhances the algorithm with the capability of local grid adaptation, based on the splitting of the existing elements into new ones. Special treatment is needed for hybrid grids, due to the variety of element types (tetrahedral, prismatic and pyramidical) and their division alternatives. The algorithm is validated against benchmark test cases, proving its potential for improving the accuracy with the implementation of the afore-mentioned techniques.*

1 INTRODUCTION

As radiative heat transfer is a major mode of heat transfer in many engineering and industrial applications, many researchers have been devoted in the development of computational methods for the prediction of heat transfer due to radiation. Among the developed ones, the Finite-Volume Method (FVM), initially proposed by Raithby and Chui [1], has gained some popularity solving radiative heat transfer problems, because of its simplicity and its ability to be implemented in complex geometries. Considering these characteristics, this method has been widely employed in the prediction of radiative heat transfer in various shapes of enclosures, described by structured or unstructured tetrahedral (triangular for 2D), hybrid or polygonal grids and cartesian or cylindrical coordinates [2-12]. Additionally, it possesses another attractive feature, the treatment of radiation in a similar to flow way, as the formulation and the solution of the discrete equations is a common procedure for fluid flow and radiation [2, 11, 12, 13]. Therefore, it proves to be especially familiar for Computational Fluid Dynamics (CFD) scientists, compared for example with Monte-Carlo method, which is based on view factors, requiring as such additional knowledge and experience [12, 13]. Nevertheless, two shortcomings of the FVM have been mainly identified, reducing the accuracy of its results, namely, the ray effect and false scattering [14-16]. The first is associated with the angular discretization, while its effects can be mitigated by the utilization of more finite control angles [14]. The second one, studied in this work, is associated with the spatial discretization and corresponds to the false or numerical diffusion in CFD [15], while its effects can be subdued in general by using finer grids or more accurate spatial schemes [16].

Considerable efforts have been exerted for the development of algorithms, encountering effectively the false scattering by employing higher order accurate spatial schemes [15, 16]. Although such a practice is common in the computation of the convective fluxes of the Navier-Stokes equations in CFD, it is rarely implemented for the evaluation of the radiative heat fluxes [16]. For a first order scheme, the evaluation of the numerical fluxes in each face of a control volume, which corresponds to an edge connecting adjacent nodes in the node-centered scheme, is based on the values at these end-points. On the contrary, a second order scheme takes into account the values of more mesh nodes, by reconstructing the values of the two end-nodes with the Taylor series expansions, such as in the MUSCL (Monotonic Upstream Scheme for Conservation Laws) technique [17]. In addition, a slope limiter, such as Van Albada-Van Leer [17, 18] and Min-mod [17, 19], should accompany the higher order scheme in order to control the total variation of the reconstructed field and assure the monotonicity between the two states of the interface of the control volumes. Moreover, a second order scheme can sometimes derive negative unphysical values of radiative intensity, which are usually mitigated by a fix-up procedure [16]. However, such a remedy along with the common practice solving the Radiative Transfer Equation (RTE) with simple iterative approximations [11, 12] can lead to oscillations or even to the failure of the solution. In order to face this deficiency, the time-dependent RTE [20-22] can be employed for a pseudo-transient simulation in conjunction with a more accurate temporal scheme, such as the Runge-Kutta method [23], considering that a higher order spatial scheme shall be accompanied by an also higher order temporal method.

As stated already, the mitigation of false scattering can be succeeded with the utilization of finer grids, requiring increased computational effort. Considering that for many practical problems some phenomena are sufficiently localized, grid adaptation can be employed to increase the spatial resolution and consequently the accuracy of the results in a specific region, without increasing significantly the memory and computational requirements [24-27]. In general, grid adaptation methods can be divided in two categories, namely redistribution and re-

finement [27]. In the first category of methods, the nodes are repositioned in order a finer discretization to be succeeded in selected regions. Despite the conservation of the total node number, these methods encounter difficulties in cases including complex geometries. The methods of the second category are based on the addition of degrees of freedom following predefined rules, as the h-refinement, implemented in this study. The mesh is enriched by dividing the existing elements into new ones; the procedure begins with the selection of the area for enrichment, using appropriate criterions, and continues with the division of the corresponding edges, faces and elements of this area. Special treatment is needed for hybrid meshes, due to the variety of the element types (hexahedral, tetrahedral, prismatic and pyramidical) and their division alternatives. Except for the previous categorization, mesh adaptation methods can be divided according to the type of the grid (hybrid or tetrahedral) [24, 27] or the type of the computational system (serial or parallel) [26].

In this study, a second order accurate spatial/temporal scheme along with the h-refinement technique is developed to enhance a parallelized node-centered finite-volume algorithm for the prediction of radiative heat transfer in three-dimensional unstructured hybrid grids, including absorbing-emitting and scattering mediums [11, 12]. Our main aim is to improve the accuracy of the algorithm in relatively coarse meshes, in which a first order accurate spatial scheme imports non-negligible false scattering amounts. As such, a second order spatial scheme, based on the MUSCL reconstruction of the radiative intensity values, along with the Van Albada-Van Leer and the Min-mod slope limiters, is incorporated. In order to avoid oscillations, derived by the second order spatial scheme in conjunction with the fix-up procedure and the standard iterative solution of the non time-dependent RTE, a second order accurate in time Runge-Kutta method is employed for the solution of the corresponding time-dependent equation. In addition, the h-refinement technique is included to increase the spatial resolution locally in selected areas of unstructured hybrid grids, including tetrahedral, prismatic, and pyramidical elements (the latter utilized only in the transition region of the grid from the prismatic to the tetrahedral elements). The relatively increased requirements for memory and computational effort, derived from the previous methods, are subdued by the utilization of an edge-based data structure along with a parallelized implementation, based on the domain decomposition approach and MPI (Message Passing Interface) [11, 12]. Finally, the proposed numerical approach is validated against benchmark test cases, confirming its capability to mitigate false scattering and consequently improve the accuracy of the solution in coarse computational grids. This feature makes relatively negligible the increase of the computational requirements, derived by the incorporation of the second order accurate spatial/temporal scheme and the h-refinement method.

2 MATHEMATICAL ANALYSIS

2.1 Governing equation and discretization

The radiative intensity for an absorbing, emitting and scattering gray medium at any node P in position $\vec{r}$ along a path $\hat{s}$ can be calculated either for steady-state or transient simulations by the time-dependent RTE [20] as:

$$\frac{1}{c}\frac{dI_P(\vec{r},\hat{s})}{dt}+\frac{dI_P(\vec{r},\hat{s})}{ds}=-\beta I_P(\vec{r},\hat{s})+k_\alpha I_b(\vec{r})+\frac{\sigma_s}{4\pi}\int_{4\pi} I_P'(\vec{r},\hat{s}_i')\Phi(\hat{s},\hat{s}_i')d\omega \qquad (1)$$

where I_P is the radiative intensity of node P, c is the propagation speed of radiation in the medium, β ($\beta=k_\alpha+\sigma_s$) is the extinction coefficient, k_α is the absorption coefficient, σ_s is the scattering coefficient and I_b is the black body intensity, based on the temperature of the medium

in the position $\vec{r}$. As such, the left hand side terms of the RTE express the rate of change of the intensity in time t and in position/direction $\vec{r}$, $\hat{s}$, the latter defined in this study by the polar and azimuthal angles θ and φ, respectively. The first right hand side term expresses the attenuation by absorption and scattering to other directions, while the second one the black body emission. Finally, the third term, which is described by the Scattering Phase Function (SPF) $\Phi\left(\hat{s},\hat{s}_i'\right)$, represents the radiation obtained by scattering from the other directions [11, 12, 13].

As far as the discretization is concerned, the RTE has to be solved for a discrete number of finite solid angles (angular discretization) and a discrete number of finite control volumes (spatial discretization). The finite solid angles, in which the directional domain is divided for the angular discretization, are defined usually by lines of constant longitude and constant latitude on the surface of a sphere (Figure 1) [11, 13]. For the spatial discretization, a node-centered scheme is utilized in this study, in accordance with which the median control volume of a node is constructed by connecting lines defined by edge midpoints, barycenters of faces and barycenters of elements, sharing this node [11, 28]; the contributions to the control volume of a node P from different types of elements (prismatic, pyramidical and tetrahedral) adjacent to this node are illustrated in Figure 2.

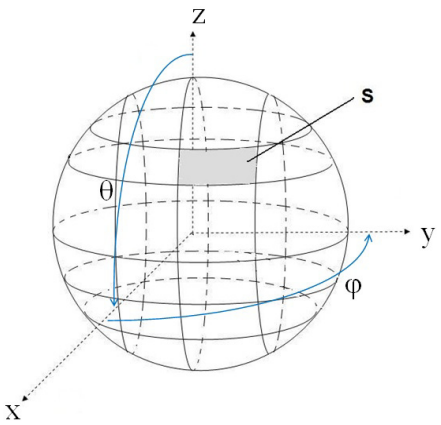

Figure 1: Angular discretization.

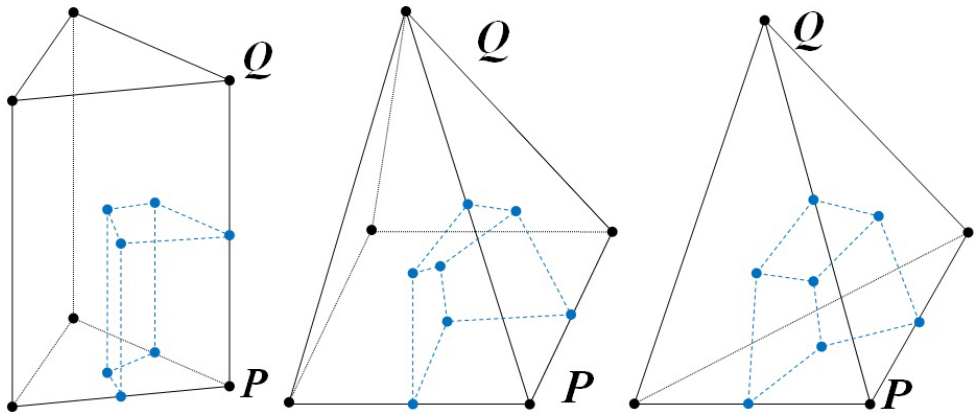

Figure 2: Contributions of three different types of elements (prismatic, pyramidical and tetrahedral) to the control volume of a node P.

2.2 Formulation of discrete equations

Considering the discretization schemes (spatial and angular) of the previous paragraph, the RTE is integrated for a node P over its spatial finite control volume V_P and over a finite solid

angle Ω^{mn}, while subsequently (with the implementation of the divergence theorem) it is formulated as:

$$\Delta I_P^{mn} \frac{V_P \Delta\Omega^{mn}}{c\Delta t} + \sum_i I_i^{mn} D_{ci}^{mn} \Delta A_i = \left[-\beta I_P^{mn} + S_R^{mn} \right] V_P \, \Delta\Omega^{mn} \tag{2}$$

where D_{ci}^{mn} is the directional weight of the solid angle *mn* and the surface *i* of the control volume, while S_R^{mn} is the sum of the emissive and in-scattering terms, which are defined as [6, 11]:

$$D_{ci}^{mn} = \int_{\theta^{m-}}^{\theta^{m+}} \int_{\varphi^{n-}}^{\varphi^{n+}} \left(\hat{s} \cdot \hat{n}_i \right) \sin\theta \, d\theta \, d\varphi \tag{3}$$

$$\hat{s} = \sin\theta \, \cos\varphi \, \hat{e}_x + \sin\theta \, \sin\varphi \, \hat{e}_y + \cos\theta \, \hat{e}_z \tag{4}$$

$$\hat{n}_i = n_x \hat{e}_x + n_y \hat{e}_y + n_z \hat{e}_z \tag{5}$$

$$\Delta\Omega^{mn} = \int_{\theta^{m-}}^{\theta^{m+}} \int_{\varphi^{n-}}^{\varphi^{n+}} \sin\theta \, d\theta \, d\varphi \tag{6}$$

$$S_R^{mn} = k_\alpha I_b + \frac{\sigma_s}{4\pi} \int_{4\pi} I_P^{m'n'} \, \Phi\left(m'n', mn \right) \, d\omega = k_\alpha \frac{\sigma T^4}{\pi} + \frac{\sigma_s}{4\pi} \sum_{m_i'=1}^{N_\theta} \sum_{n_i'=1}^{N_\varphi} I_P^{m_i' n_i'} \bar{\Phi}\left(m_i' n_i', mn \right) \Delta\Omega^{m_i' n_i'} \tag{7}$$

Quantity $\bar{\Phi}\left(m_i' n_i', mn \right)$ is the average scattering phase function, expressing the scattering contribution of the control angle $m_i' n_i'$ (incident angle) to the control angle *mn* (in-scattering angle) [11]; for isotropic scattering it is assumed equal to unity, while for anisotropic one its value depends on the utilized model (i.e. Legendre polynomials) [11, 29, 30, 31]. Though the angles θ^m and φ^n can be defined arbitrarily, they are obtained from the equal division of the 4π steradians into $N_\theta \times N_\varphi$ directions, such that $\Delta\theta^m = \theta^{m+} - \theta^{m-} = \pi / N_\theta$ and $\Delta\varphi^n = \varphi^{n+} - \varphi^{n-} = 2\pi / N_\varphi$ [6, 11]. Considering this angular discretization, the directional weight D_{ci}^{mn} and the discrete control angle $\Delta\Omega^{mn}$ can be evaluated as:

$$\begin{aligned}
D_{ci}^{mn} &= D_{ci,x}^{mn} + D_{ci,y}^{mn} + D_{ci,z}^{mn} = \int_{\theta^{m-}}^{\theta^{m+}} \int_{\varphi^{n-}}^{\varphi^{n+}} \left(\hat{s} \, n_x \hat{e}_x + \hat{s} \, n_y \hat{e}_y + \hat{s} \, n_z \hat{e}_z \right) \sin\theta \, d\theta \, d\varphi \\
D_{ci,x}^{mn} &= \frac{n_x}{2} \left(\sin\varphi^{n+} - \sin\varphi^{n-} \right) \left[\left(\theta^{m+} - \theta^{m-} \right) - \left(\cos\theta^{m+} \sin\theta^{m+} - \cos\theta^{m-} \sin\theta^{m-} \right) \right] \\
D_{ci,y}^{mn} &= \frac{n_y}{2} \left(\cos\varphi^{n-} - \cos\varphi^{n+} \right) \left[\left(\theta^{m+} - \theta^{m-} \right) - \left(\cos\theta^{m+} \sin\theta^{m+} - \cos\theta^{m-} \sin\theta^{m-} \right) \right] \\
D_{ci,z}^{mn} &= \frac{n_z}{2} \left(\varphi^{n+} - \varphi^{n-} \right) \left(\sin^2\theta^{m+} - \sin^2\theta^{m-} \right)
\end{aligned} \tag{8}$$

$$\Delta\Omega^{mn} = \int_{\theta^{m-}}^{\theta^{m+}} \int_{\varphi^{n-}}^{\varphi^{n+}} \sin\theta \, d\theta \, d\varphi = \left(\varphi^{n+} - \varphi^{n-} \right) \left(\cos\theta^{m-} - \cos\theta^{m+} \right) \tag{9}$$

By applying the step scheme, which resembles a simple upwind scheme in CFD, the value of the radiative intensity of a downstream face is set equal to that of the upstream node [6, 11, 12], resulting in the following expression for the second left hand side term of equation (2):

$$I_i^{mn} D_{ci}^{mn} = I_P^{mn} D_{ci,out}^{mn} + I_Q^{mn} D_{ci,in}^{mn} \tag{10}$$

In structured meshes the application of the previous equation is straightforward, as the angular discretization is selected to match exactly with the control volumes' faces. On the contrary, in unstructured grids the control angles are inevitably overlapped [6, 11, 12], requiring appropriate manipulation for a more accurate solution, such as the bold approximation and the pixelation method. According to the first approximation, an overhang solid angle is considered wholly either outgoing or incoming, depending on the sign of its directional weight [11] (Figure 3a-b). Considering this remedy for the overhang problem, the directional weights of equation (10) are defined as:

$$\begin{aligned} D_{ci,out,bold}^{mn} &= \alpha_{ci,bold}^{mn} \left| \left(D_{ci}^{mn} \right) \right| \\ D_{ci,in,bold}^{mn} &= -\left(1 - \alpha_{ci,bold}^{mn} \right) \left| \left(D_{ci}^{mn} \right) \right| \\ \alpha_{ci,bold}^{mn} &= \begin{cases} 1 \;\; if \;\; D_{ci}^{mn} \geq 0 \\ 0 \;\; if \;\; D_{ci}^{mn} < 0 \end{cases} \end{aligned} \tag{11}$$

where $\alpha_{ci,bold}^{mn}$ is the approach coefficient for the directional weight D_{ci}^{mn}. Respectively, in the pixelation approach each control angle is divided in smaller ones, for which the bold approximation is employed [6] (Figure 3c), resulting in the following expressions for the directional weights:

$$\begin{aligned} D_{ci,out,pix}^{mn} &= \alpha_{ci,pix}^{mn} \sum_{m_i=1}^{N_m} \sum_{n_i=1}^{N_n} \left| D_{ci}^{m_i n_i} \right| \\ D_{ci,in,pix}^{mn} &= -\left(1 - \alpha_{ci,pix}^{mn} \right) \sum_{m_i=1}^{N_m} \sum_{n_i=1}^{N_n} \left| D_{ci}^{m_i n_i} \right| \\ \alpha_{ci,pix}^{mn} &= \frac{\sum_{m_i=1}^{N_m} \sum_{n_i=1}^{N_n} \max\left(D_{ci}^{m_i n_i}, 0 \right)}{\sum_{m_i=1}^{N_m} \sum_{n_i=1}^{N_n} \left| D_{ci}^{m_i n_i} \right|} \end{aligned} \tag{12}$$

where $\alpha_{ci,pix}^{mn}$ is the corresponding approach coefficient, calculated by the sum of the positive subangles' directional weights, divided by the sum of the absolute values of them. Although this approximation is usually applied only in the overhang control angles of the nodes [2, 6], in this study it is implemented to all the nodes and control angles in a pre-computation stage. As the values of those coefficients and directional weights do not vary during the iterative solution of the RTE, they are evaluated before the beginning of the procedure, assuring a reduced computation time per iteration. As such, the RTE is reformulated independently of the employed approximation as:

$$\Delta I_P^{mn} \frac{V_P \Delta\Omega^{mn}}{c\Delta t} = \left[-\beta I_P^{mn} + S_R^{mn} \right] V_P \Delta\Omega^{mn} - \sum_i I_P^{mn} D_{ci,out}^{mn} \Delta A_i - \sum_i I_Q^{mn} D_{ci,in}^{mn} \Delta A_i \tag{13}$$

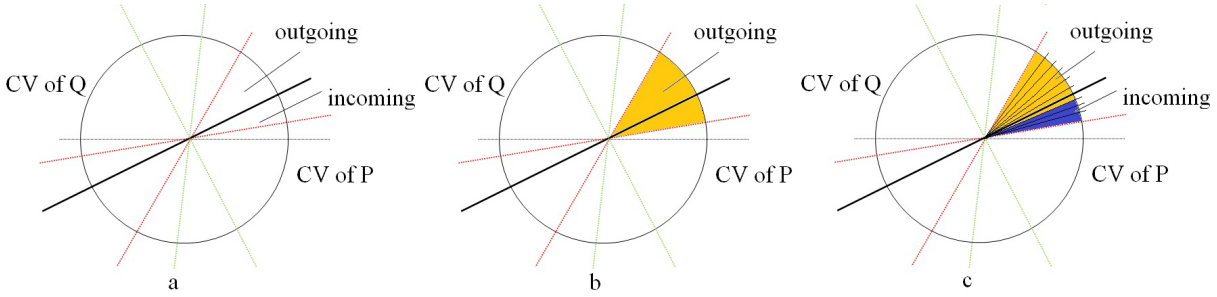

Figure 3: a) Schematic of the control angle overhang problem. b) Implementation of the bold approximation. c) Implementation of the pixelation method.

Boundaries' contributions have also to be considered in the corresponding nodes' flux balances, in order their equation sets to be admissible for solution. The boundary conditions in radiative heat transfer concern walls, inlets, outlets and symmetric planes; the first three types are managed in the same way, as opaque and diffuse surfaces, while for the last one a slightly different manipulation is required. As such, the wall boundary conditions are usually implemented in an explicit way (Dirichlet), assigning to the boundary nodes intensity values, computed as the sum of their blackbody intensity, due to their temperature, and the reflection of the incoming intensities [2, 6, 11, 12]. Despite the common practice, these boundary conditions are applied implicitly in this study, implementing the step scheme between the boundary node and a "ghost" node outside the grid. Considering this manipulation, equation (13) for a boundary node P is defined as:

$$\begin{aligned} &\Delta I_P^{mn} \frac{V_P \Delta\Omega^{mn}}{c\Delta t} = \left[-\beta I_P^{mn} + S_R^{mn} \right] V_P \, \Delta\Omega^{mn} \\ &-\sum_i I_P^{mn} \left(D_{ci,out}^{mn} \Delta A_i + D_{ci,out,w}^{mn} \Delta A_w \right) - \sum_i \left(I_Q^{mn} D_{ci,in}^{mn} \Delta A_i + I_w^{mn} D_{ci,in,w}^{mn} \Delta A_w \right) = R_P^{mn} \end{aligned} \tag{14}$$

where $D_{ci,out,w}^{mn}$ is the directional weight going outward of the control volume of node P and $D_{ci,in,w}^{mn}$ is the corresponding directional weight coming inwards to the same control volume. Depending on the employed bold or pixelation scheme, such directional weights are calculated using either equation (11) or (12). For the computation of the radiative intensity of the "ghost" node, I_w^{mn}, which appears in the previous equation, the following equation is utilized:

$$I_w^{mn} = \varepsilon_w I_{b,P} + \frac{1-\varepsilon_w}{\pi} \sum_{m_i=1}^{N_\theta} \sum_{n_i=1}^{N_\varphi} I_P^{m_i n_i} D_{ci,out,w}^{m_i n_i} \tag{15}$$

As far as the symmetry boundary conditions are concerned, the same implicit scheme is applied, evaluating radiative intensity of the "ghost" node, I_w^{mn}, such as the net heat flux become zero at the symmetry plane, resembling in that way a specularly reflecting wall [32]. Therefore, the intensities of such a boundary node, going out of its control volume to the symmetry plane, are placed as incoming in its control volume in the mirroring direction. Employing mirroring boundary conditions, which is commonly met in CFD, results in reduced memory and computational requirements, due to the smaller utilized mesh. Nevertheless, for its implementation, the angular discretization should be appropriately performed, in order the mirroring plane to coincide with a discrete solid angle limit; otherwise an interpolation scheme should be employed [32].

2.3 Time integration

An explicit scheme, using a four stage Runge-Kutta (RK(4)) method, is implemented for the time integration of the RTE and its iterative solution as follows [17, 23]:

$$\begin{aligned}
&\Delta I_P^{mn} \frac{V_P \Delta\Omega^{mn}}{c\Delta t_P} = R_P^{mn} \\
&\left(I_P^{mn}\right)^{l+1,0} = \left(I_P^{mn}\right)^{l} \\
&\left(I_P^{mn}\right)^{l+1,k} = \left(I_P^{mn}\right)^{l} + \alpha_k \frac{c\Delta t_P}{V_P \Delta\Omega^{mn}} R_P^{mn}\left(\left(I_P^{mn}\right)^{l+1,k-1}\right),\ k = 1,\ldots,4 \\
&\left(I_P^{mn}\right)^{l+1} = \left(I_P^{mn}\right)^{l+1,4}
\end{aligned} \tag{16}$$

where α_1, α_2, α_3 and α_4 are the constants of the method with values 0.11, 0.26, 0.5 and 1.0 respectively, attributing the procedure with a second order accuracy in time [17, 23]. The term l is the current external iteration number, k is the current Runge-Kutta iteration number and Δt_P is the local pseudo-time step [17, 33], based on the length $\alpha_{edge,P}$ of the shortest edge of the grid connected to the node P, which is defined for a steady-state simulation as [17, 20]:

$$c\Delta t_P \le \frac{1}{2}\min(\alpha_{edge,P}) \tag{17}$$

Employing the local pseudo-time stepping scheme, a common practice in steady-state CFD simulations, accelerates the convergence of the iterative solution, as for each node the maximum permissible time step is utilized [17]. Nevertheless, for transient-unsteady simulations a global time step should be applied instead, computed as the smaller of the local ones. In case the iterative procedure derives a negative unphysical value of intensity (usually in the initial iterations along with a higher order spatial scheme), a fix-up procedure is implemented, setting this value equal to zero [16]. Once the new intensity values are calculated, they should be exchanged between the adjacent subdomains for a parallelized implementation of the algorithm [11, 12].

3 HIGH ORDER SPATIAL SCHEME

For a first order accurate spatial scheme the left and right states of a face of a control volume of a node P, which coincides with an edge PQ in the node-centered scheme, are approximated by the values at the end-points of the edge. However, for a higher order scheme, these states are defined by the reconstructed values of the same nodes implementing the Taylor series expansions; the MUSCL scheme is employed in this study, accompanied with a slope limiter to control the total variation of the reconstructed field [17, 18, 19, 34]. Considering this approximation, the left and right values at the midpoint of an edge PQ are defined as [17, 34]:

$$\begin{aligned}
\left(I_{PQ}^{mn}\right)^{L} &= I_P^{mn} + \frac{1}{2}\left(\nabla I^{mn}\right)_P \vec{r}_{PQ} \\
\left(I_{PQ}^{mn}\right)^{R} &= I_Q^{mn} - \frac{1}{2}\left(\nabla I^{mn}\right)_Q \vec{r}_{PQ}
\end{aligned} \tag{18}$$

where $\vec{r}_{PQ}$ is the vector connecting the end-nodes P and Q. For the calculation of the extrapolation gradients $(\nabla I^{mn})_P$ and $(\nabla I^{mn})_Q$ at these end-points, the Green-Gauss linear representation method is employed, described as [17, 34]:

$$\left(\nabla I^{mn}\right)_P = \frac{1}{V_P}\left(\sum_{i,edge\,PQ} \frac{1}{2}\left(I_P^{mn} + I_Q^{mn}\right)\hat{n}_i \Delta A_i + \sum_{i,P-wall} I_P^{mn} \cdot \hat{n}_{i,w} \Delta A_w \right) \tag{19}$$

where the last term of the equation is activated only in case the node *P* is a boundary one. Once these gradients are computed, they should be exchanged between the adjacent subdomains for a parallelized implementation of the algorithm [11, 12, 35, 36, 37]. Considering equation (18), equation (10), describing the step scheme, is reformulated as:

$$I_i^{mn} D_{ci}^{mn} = \left(I_{PQ}^{mn}\right)^L D_{ci,out}^{mn} + \left(I_{PQ}^{mn}\right)^R D_{ci,in}^{mn} \tag{20}$$

As stated before, a slope limiter is required, in order the total variation in the reconstructed field to be minimized; the Van Albada-Van Leer (VLVA) [17, 18] and the Min-mod [17, 19] are included in the present study. They are both based on the centered $\left(\nabla I_{PQ}^{mn}\right)^c$ and the upwind $\left(\nabla I_P^{mn}\right)^u$,$\left(\nabla I_Q^{mn}\right)^u$ gradients, defined as [18, 19]:

$$\begin{aligned} \left(\nabla I_{PQ}^{mn}\right)^c \cdot \vec{r}_{PQ} &= I_Q^{mn} - I_P^{mn} \\ \left(\nabla I_P^{mn}\right)^u &= 2\left(\nabla I_P^{mn}\right) - \left(\nabla I_{PQ}^{mn}\right)^c \\ \left(\nabla I_Q^{mn}\right)^u &= 2\left(\nabla I_Q^{mn}\right)^u - \left(\nabla I_{PQ}^{mn}\right)^c \end{aligned} \tag{21}$$

while their utilization transforms equation (18), which derives the reconstructed values of the left and right states of the examined edge *PQ,* as follows:

$$\begin{aligned} \left(I_{PQ}^{mn}\right)^L &= I_P^{mn} + \frac{1}{2} \cdot X\left(\left(\nabla I_P^{mn}\right)^u \cdot \vec{r}_{PQ}, \left(\nabla I_{PQ}^{mn}\right)^c \cdot \vec{r}_{PQ}\right) \\ \left(I_{PQ}^{mn}\right)^R &= I_Q^{mn} - \frac{1}{2} \cdot X\left(\left(\nabla I_Q^{mn}\right)^u \cdot \vec{r}_{PQ}, \left(\nabla I_{PQ}^{mn}\right)^c \cdot \vec{r}_{PQ}\right) \end{aligned} \tag{22}$$

where X is the limiter function, defined for the Van Albada-Van Leer limiter as [18]:

$$X(a,b) = \begin{cases} \dfrac{(a^2+e)b + (b^2+e)a}{a^2+b^2+2e} & ab > 0 \\ 0 & ab \le 0 \end{cases} \tag{23}$$

and for the Min-mod limiter as [19]:

$$X(a,b) = \begin{cases} a \text{ if } |a| < |b| \text{ and } ab > 0 \\ b \text{ if } |b| < |a| \text{ and } ab > 0 \\ 0 \qquad\qquad \text{if } ab \le 0 \end{cases} \tag{24}$$

where *e* is a very small number with a typical value of 10^{-16} to prevent division by zero. If the second order scheme derives a negative unphysical intensity (usually in the initial iterations), the first order scheme is employed instead. By utilizing a higher order spatial scheme, the R/H side term of equation (14) is defined as:

$$R_P^{mn} = \left[-\beta I_P^{mn} + S_R^{mn} \right] V_P \, \Delta\Omega^{mn}$$
$$-\sum_i \left(I_{PQ}^{mn} \right)^L \left(D_{ci,out}^{mn} \Delta A_i + D_{ci,out,w}^{mn} \Delta A_w \right) - \sum_i \left(\left(I_{PQ}^{mn} \right)^R D_{ci,in}^{mn} \Delta A_i + I_w^{mn} D_{ci,in,w}^{mn} \Delta A_w \right) \quad (25)$$

4 GRID ADAPTATION

Except for the second order accurate schemes, false scattering can be reduced by utilizing finer grids, which however call for increased memory requirements and computational effort. Local grid refinement techniques can be applied during the solution procedure to increase the accuracy in preselected regions along with significant computational savings, as they avoid the generation of new meshes from scratch. Such methods are widely employed in CFD simulations, especially in cases including sufficiently localized phenomena as shocks or in cases encountered for the first time in which no previous knowledge exists about the necessary spatial accuracy. Considering the above states the serial h-refinement method is incorporated in the present algorithm, which concerns the enrichment of the grid with new nodes as midpoints of the edges positioned in the targeted area, along with the division of those edges and the corresponding faces and elements.

The h-refinement technique can be divided basically in three main steps: a) The detection of the desired areas for adaptation and the marking of the corresponding edges for division, which is succeeded by defining appropriate criterions, targeting usually regions of the field with high gradients of a specific variable or regions with a specific characteristic. b) The spread of marking information to the neighboring edges, as the marking derived by the first step cannot lead to an admissible refinement pattern for the construction of the new mesh; the neighboring edges to the marked ones have to be examined by looping several times over the elements of the mesh [27]. This edge-based structure makes h-refinement particularly attractive for implementation in hybrid grids, including various types of elements. c) The embedding of new nodes as midpoints of the marked edges and the division of these edges; the corresponding faces and elements are divided then accordingly [27]. The whole procedure is based on some predefined rules, which are described as follows:

1. Every new, embedded as midpoint of an edge, node of the grid is a common point of all the neighbouring faces and elements.

2. Every new edge is a common edge of all the neighbouring elements.

3. There are five permitted ways for the division of a tetrahedron (Figure 4), resulting in [24, 25, 26, 27]: a) two new tetrahedrons, b) four new tetrahedrons, c) eight new tetrahedrons, d) two new tetrahedrons, one new pyramid and one new prism and e) one new tetrahedron and one new pyramid. The last two ways (*d* and *e*) are required only in the transitional region of the grid, from the prismatic to the tetrahedral elements [11, 12], while the third division type *c* can be implemented in three possible ways, depending on the selection of the internal diagonal edge; the shortest one should always be chosen in order not to produce distorted tetrahedrons [27].

4. There are two permitted ways for the division of a prism (Figure 5), resulting in two and four new prisms respectively [24, 25, 26].

5. There are three permitted ways for the division of a pyramid (Figure 6), producing [24, 25, 26]: a) two new pyramids, b) three new prisms and a new pyramid and c) a new prism and a new pyramid.

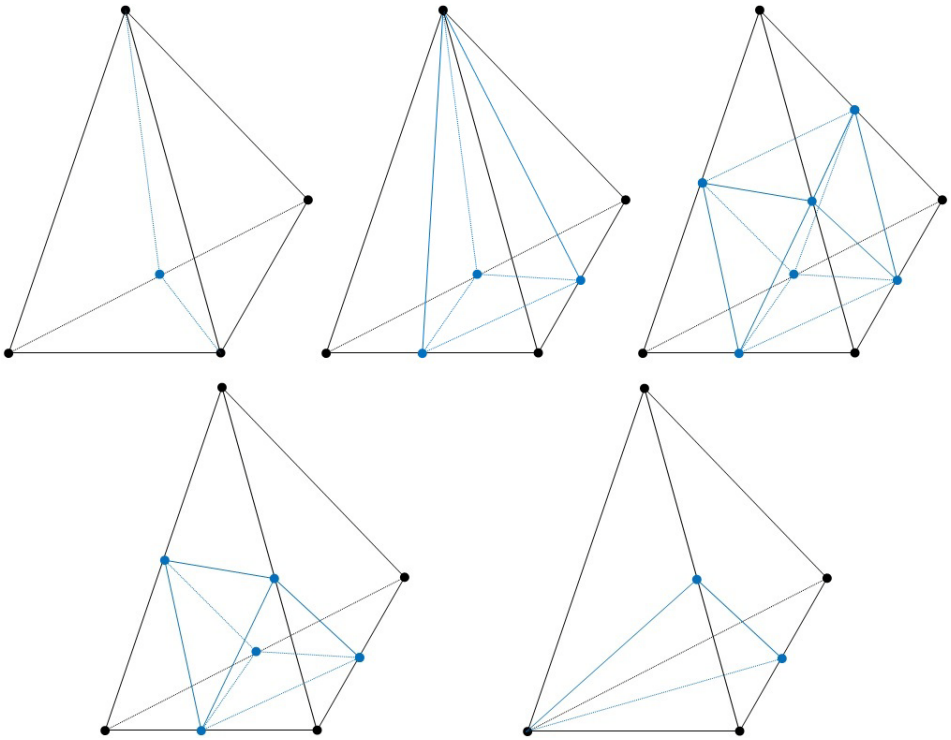

Figure 4: Permitted ways for the division of tetrahedrons.

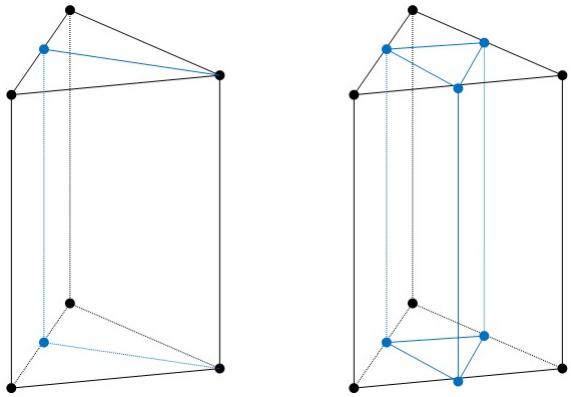

Figure 5: Permitted ways for the division of prisms.

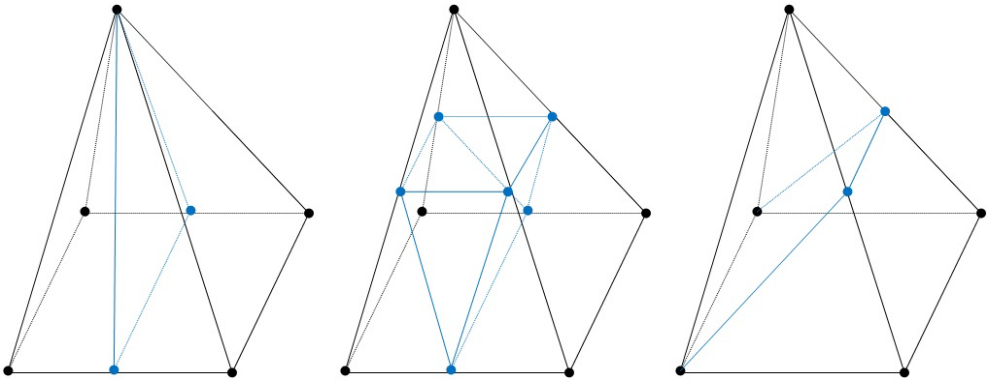

Figure 6: Permitted ways for the division of pyramids.

6. A triangular face can be divided in two or four new triangular faces, while a rectangular one can be divided only in two new rectangular faces [27].

7. The coordinates and the variables associated with a new node are defined as the arithmetic averages of the respective values at the two end-points of the edge.

5 EVALUATION

The present algorithm has been validated against benchmark test cases, comparing its results with the corresponding ones of reference solvers. The comparison is succeeded via the distributions of dimensionless incident radiative heat flux $Q^*(\vec{r})$ of the present and the reference solvers, defined as [38]:

$$Q^*(\vec{r}) = \frac{Q(\vec{r})}{\mathrm{E}} = \frac{\int_{4\pi} I(\vec{r},\hat{s})\cdot(\hat{s}\cdot\hat{n}_i)\,d\omega}{\sigma T^4} \tag{26}$$

where $Q(\vec{r})$ is the incident radiative heat flux in position $\vec{r}$, while E is the initial radiative energy, responsible for the heat transfer [11, 12]. The numerical results were obtained after the radiative intensity residual is decreased at least four orders of magnitude, computed as:

$$res = \frac{\sum_{P=1}^{N_P}\sum_{m=1}^{N_\theta}\sum_{n=1}^{N_\varphi}\left|I_P^{mn,l+1} - I_P^{mn,l}\right|}{N_P} \tag{27}$$

where N_P is the number of nodes of the whole mesh. In the next paragraphs evaluation cases including radiative heat transfer via an isothermal gray medium in a hexahedral, a J-shaped and a baffled cubic enclosure are presented.

5.1 A hexahedral enclosure with trapezoidal bases

The first quasi-3D benchmark test case considers radiative heat transfer in a hexahedral enclosure with trapezoidal bases, as illustrated in Figure 7. Two subproblems were encountered for this enclosure on a DELL(R) T7400 workstation with 2 Intel(R) Xeon(R) E5410 4-core processors at 2.33GHz.

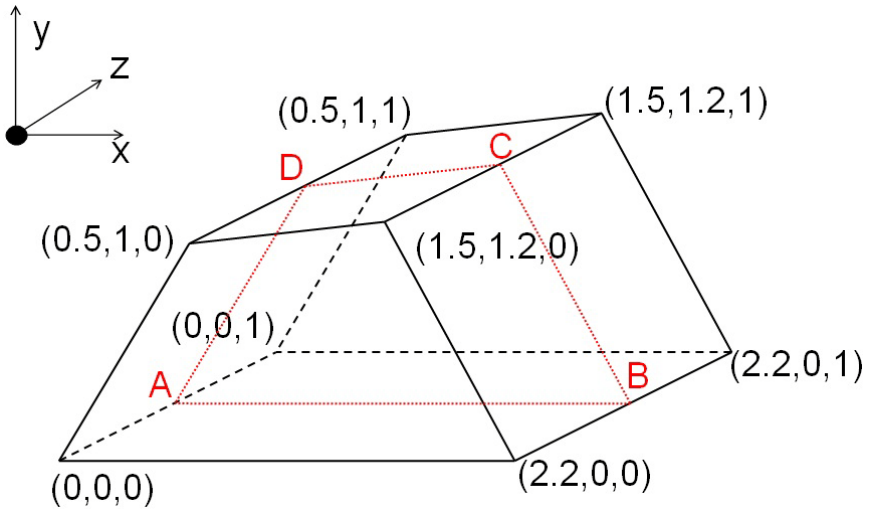

Figure 7: Dimensions of the hexahedral enclosure with trapezoidal bases.

For the first subcase, the enclosure is assumed to be composed by radiatively black (ε=1) and cold walls (T_w=0 K), except for the two trapezoidal bases (z=0 and z=1), in which symme-

try boundary conditions are imposed. The included medium is considered absorbing and emitting, but no scattering (σ=0 m^{-1}), maintained at constant temperature (T_m=100 K) with an absorbing coefficient equal to unity (k_α=1 m^{-1}). The utilized initial mesh includes 8,507 nodes, 12,608 tetrahedrons 10,754 prisms and 28 pyramids, while for parallelization it is decomposed in two subdomains (Figure 8). For angular discretization, the "sphere" is divided in 16 azimuthal - 4 polar angles, along with the pixelation method. In Figure 9 the distributions of dimensionless incident radiative heat flux along the A-B (left) and the B-C (right) lines of the mesh for all the available spatial schemes are illustrated, compared with the exact ones of Murthy and Mathur [39], while in Figure 10 the distributions along the C-D (left) and the D-A (right) lines are shown. The above mentioned solutions are obtained after the radiative intensity residual is decreased at least four orders of magnitude, requiring approximately two seconds per iteration for the first order spatial scheme and five seconds per iteration for the second order ones. As far as the effectiveness of the spatial schemes is concerned, the second order ones extract more accurate results comparing with the first order one; as expected the schemes jointed with limiters derive better distributions as the simple second order scheme seems to overpredict the intensity flux near the cold wall boundaries.

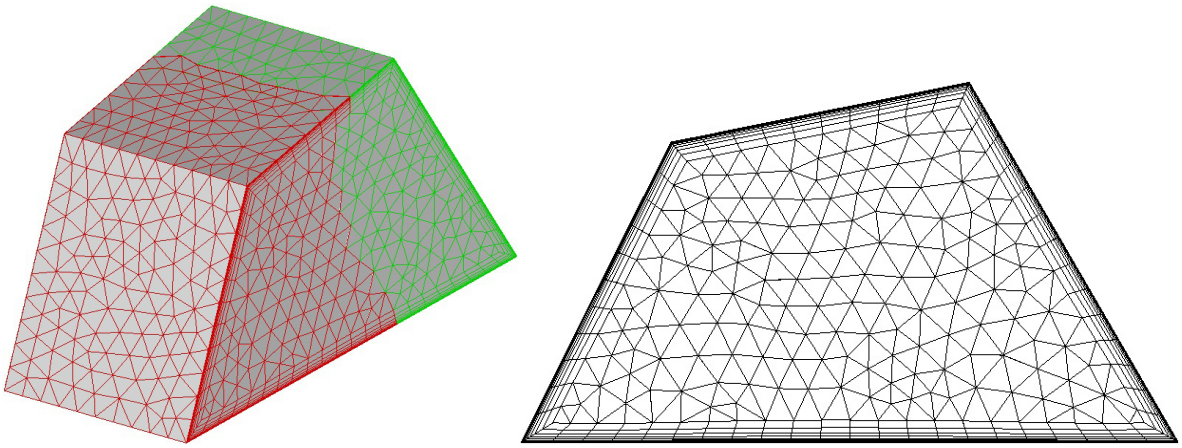

Figure 8: Utilized mesh (left) and mesh density on the face with z=0 (right) for the hexahedral enclosure.

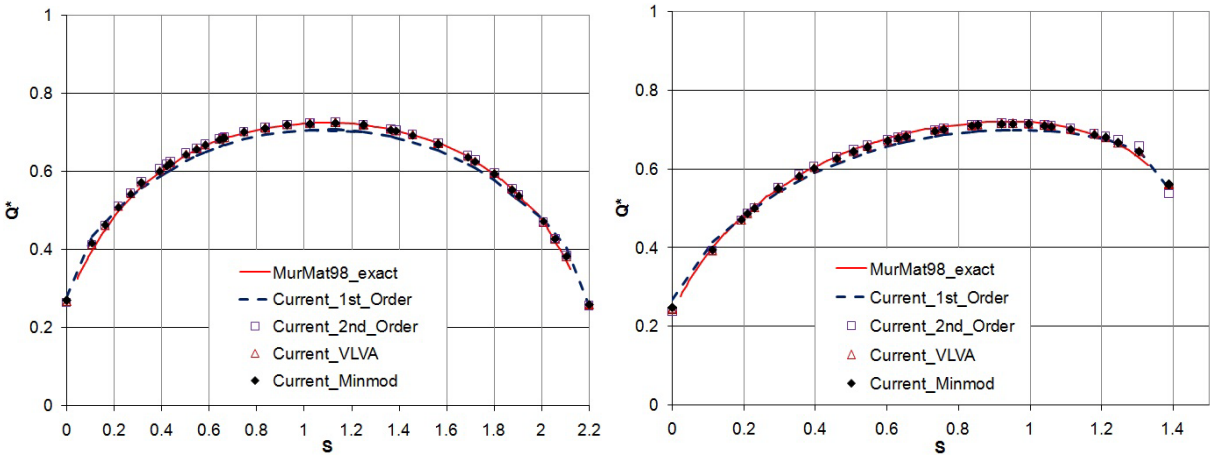

Figure 9: Distributions of dimensionless incident radiative heat flux along the A-B (left) and the B-C line (right).

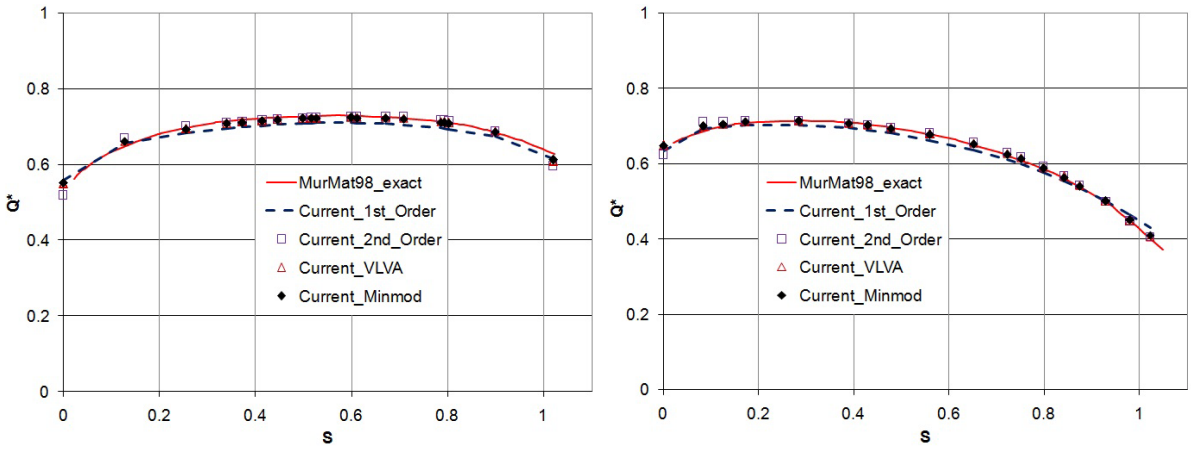

Figure 10: Distributions of dimensionless incident radiative heat flux along the C-D (left) and the D-A line (right).

In the second subcase the same conditions are imposed for the medium and the walls, except for the absorption coefficient, which takes three different values (k_α=0.1 m^{-1}, k_α=1 m^{-1}, k_α=10 m^{-1}). The utilized mesh consists of 22,788 nodes, 53,692 tetrahedrons and 23,184 prisms, while for parallelization it is decomposed in two partitions, as illustrated in Figure 11. For angular discretization 20 azimuthal and 8 polar angles are employed along with the pixelation method. The attention in this subcase is towards the evaluation of the improvement, derived by the grid adaptation. As such the current mesh is refined, utilizing a criterion which targets the region up to 0.1 m away from the cold boundaries, resulting in a new grid, consisted of 83,305 nodes, 184,522 tetrahedrons and 92,736 prisms (Figure 12). Due to that the solution, derived by the refined mesh for the case with absorption coefficient equal to 10, didn't reach the respective reference one at the regions near the cold boundaries, a second grid adaptation was performed targeting the region of these solid angles, resulting in a new mesh, composed of 190,771 nodes, 428,159 tetrahedrons and 217,812 prisms (Figure 12). All the solutions were obtained after the radiative intensity residual is decreased at least five orders of magnitude, requiring approximately twelve seconds per iteration for the initial mesh, thirty seconds for the one after the first refinement and sixty seconds for the final grid. In Figure 13 the distributions of dimensionless incident radiative heat flux along the A-B line of the initial and the refined meshes for the three absorption coefficients, are presented, compared with the corresponding exact ones of Murthy and Mathur [39].

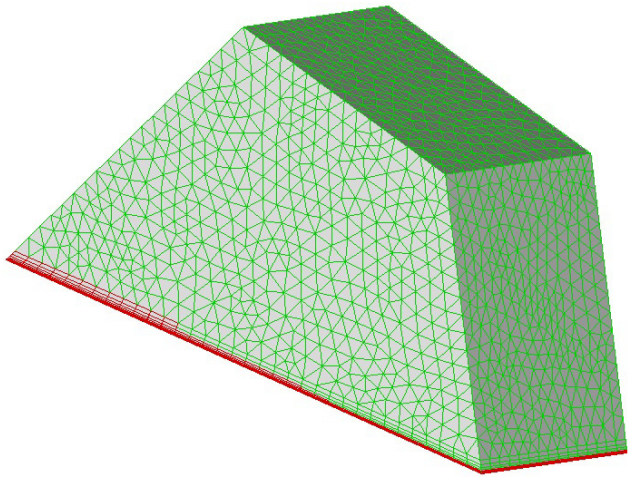

Figure 11: Utilized mesh for the hexahedral enclosure.

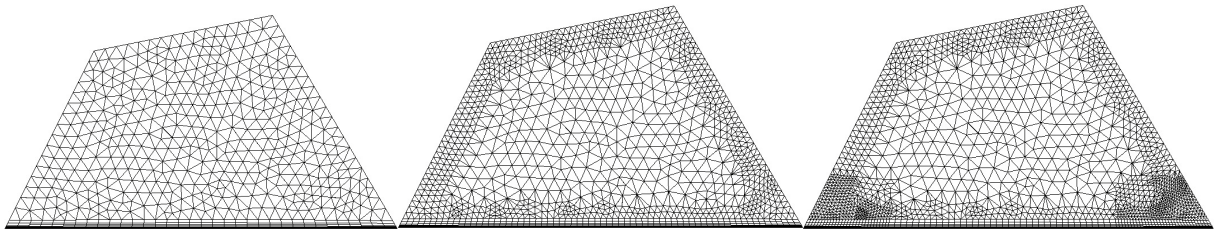

Figure 12: Mesh density on the face with z=0 before refinement, after the first refinement and after the second one.

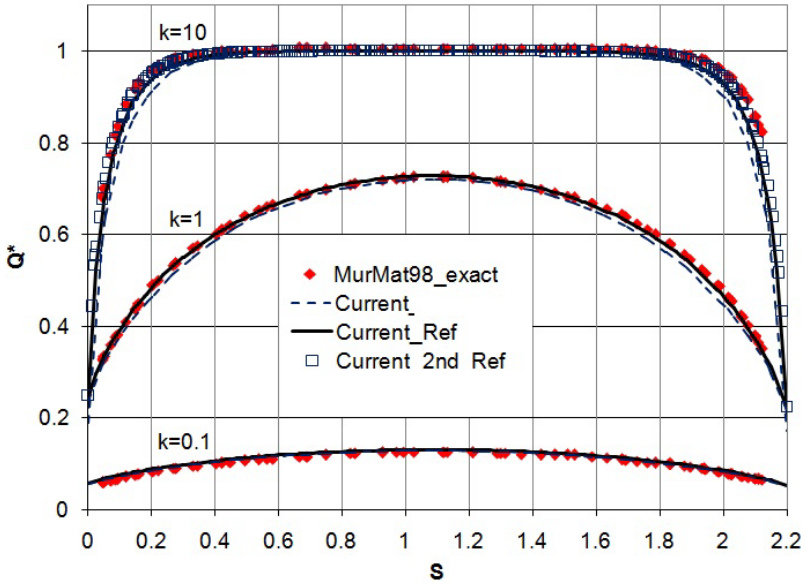

Figure 13: Distributions of dimensionless incident radiative heat flux along the A-B line for three different values of absorption coefficient, utilizing the initial and the refined meshes.

For the simulation with absorption coefficient equal to 0.1 there isn't any obvious improvement. On the contrary for the other subcases, the difference between the initial and the refined grids is evident, revealing the ability of h-refinement to derive more accurate solutions, without the need to start from the beginning the generation of a new finer grid. Although the improvement, provided by grid adaptation, isn't so important, compared to the one derived by the second order accurate schemes, it can be proved helpful, depending on the examined problem.

5.2 A J-shaped enclosure

The second test case concerns radiative heat transfer in a J-shaped enclosure, as illustrated in Figure 14. It includes an absorbing and emitting cold medium (T_m=0 K), while all the walls are considered black (ε=1) and cold (T_w=0 K), except for the upper one at y=2.4 maintained at constant temperature equal to 100K and the two bases (z=0 and z=1), in which symmetry boundary conditions are imposed. The utilized mesh is composed of 4,040 nodes, 11,132 tetrahedrons, and 2,800 prisms, while for its parallelized simulation it is divided in two partitions (Figure 15). A quite dense angular discretization of 30 azimuthal and 4 polar angles was utilized along with the pixelation approach, due to the significant ray effect, which was encountered. A value of 0.01 m^{-1} is assigned to the absorption coefficient, while the scattering coefficient remains equal to zero (σ_s=0). In Figure 16 the dimensionless incident radiative heat flux distributions along the ABCD line for all the available spatial schemes are illustrated, compared with the computed ones of Man Young Kim et al. [9]. The results were obtained

after radiative intensity residual was decreased at least four orders of magnitude, while the simulation for the first order scheme lasted about 5 minutes and for the second order ones about 14 minutes on the same to the previous case workstation. A deviation between the results of the first order scheme and the second order ones is clearly distinguished in the areas near the points A, B and C, proving the potential of the latter schemes for more accurate predictions even in relatively coarse grids. In addition, the simple second order scheme seems to mispredict slightly the radiative intensity fluxes in specific regions (i.e. point B), comparing its results with these of the schemes enhanced with limiters.

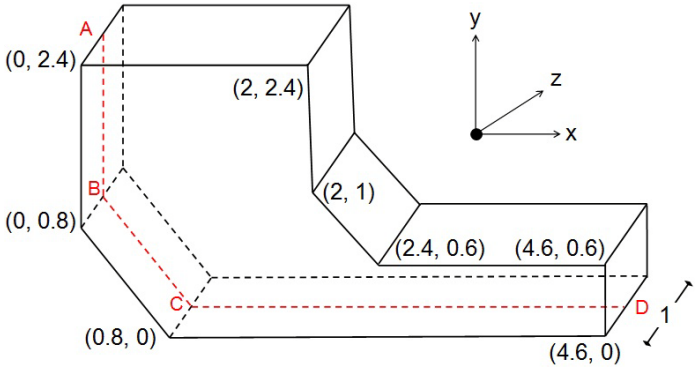

Figure 14: Dimensions of the J-shaped enclosure.

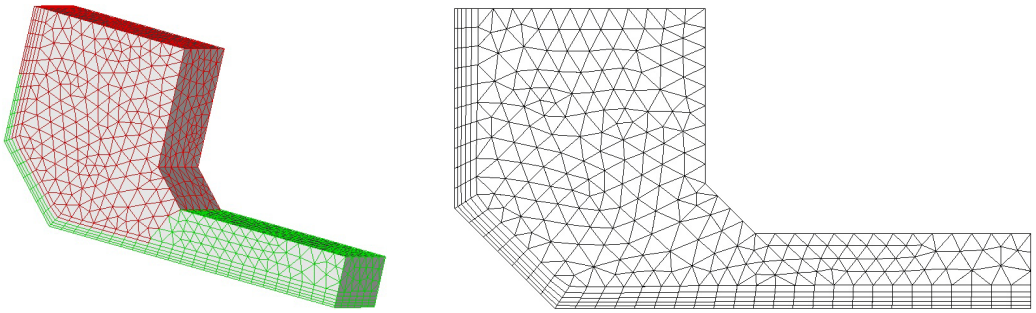

Figure 15: Utilized mesh (left) and mesh density on the face with z=0 (right).

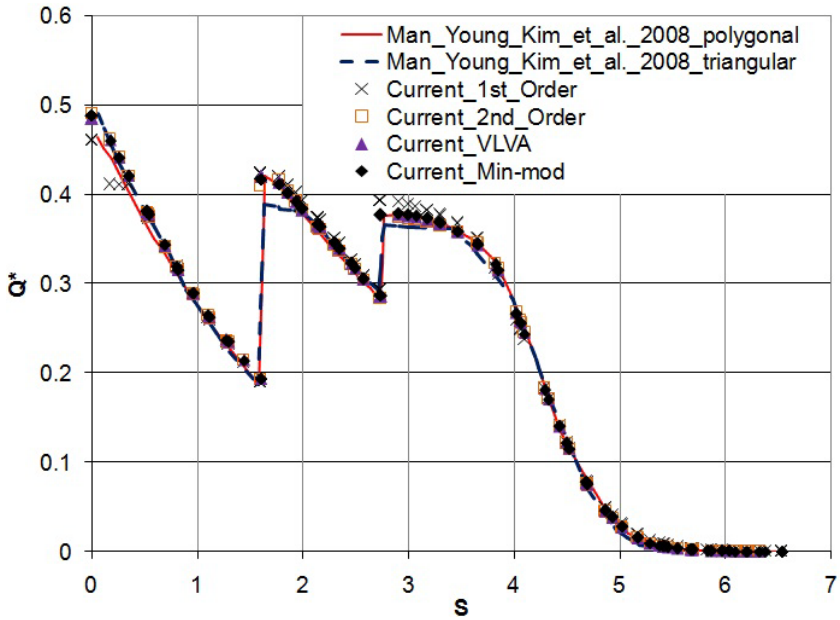

Figure 16: Distributions of dimensionless incident radiative heat flux along the ABCD line.

5.3 A cubic enclosure with three baffles

A cubic enclosure with three baffles (Figure 17), including an absorbing and emitting medium, maintaining a constant heating power E_m=10W/m^2 is examined in this case. All the walls, including the three baffles, are considered black (ε=1) with a constant emissive power E_w=1W/m^2, except for the two bases (z=0 and z=1), in which symmetry boundary conditions are imposed. The utilized mesh includes 21,228 nodes, 28,212 tetrahedrons and 29,016 prisms, while for parallelization it is divided in two subdomains (Figure 18). For angular discretization 24 azimuthal and 4 polar angles are employed along with the pixelation method. The results were extracted after radiative intensity residual was decreased at least six orders of magnitude, requiring (on a PC with an AMD FX(tm)-8120 Eight-Core Processor at 3.10 GHz) approximately five seconds per iteration for the first order scheme and fourteen seconds per iteration for the second order ones. In Figure 19 the distributions of incident radiative heat flux (Q in kW/m^2) along the ABCD line for the four available spatial schemes are illustrated, compared to the corresponding computed with Z-M (Zone-Method) ones of Coelho et al. [40]. As expected, a significant improvement to the accuracy of the computed fluxes implementing the second order schemes is identified; a slight overestimation by the simple second order scheme is observed again, unlike the schemes coupled with the limiters, due to the unbounded reconstructed values of radiative intensity.

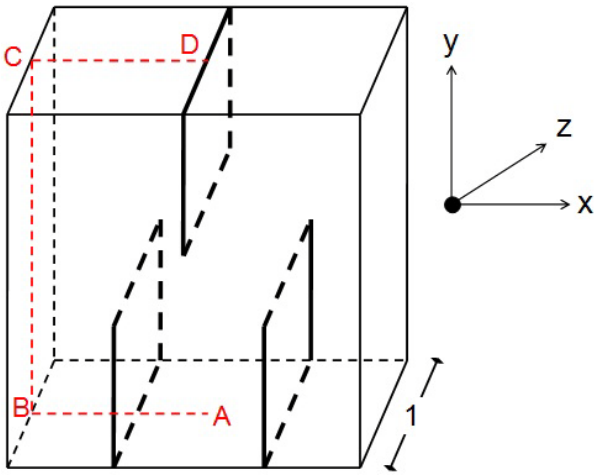

Figure 17: Dimensions of the cubic enclosure with the three baffles.

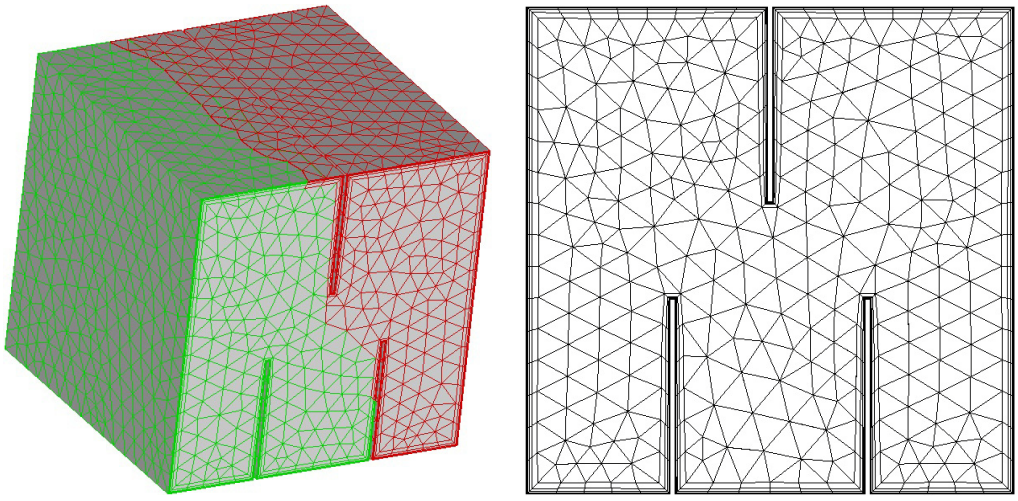

Figure 18: Utilized mesh (left) and mesh density on the face with z=0 (right).

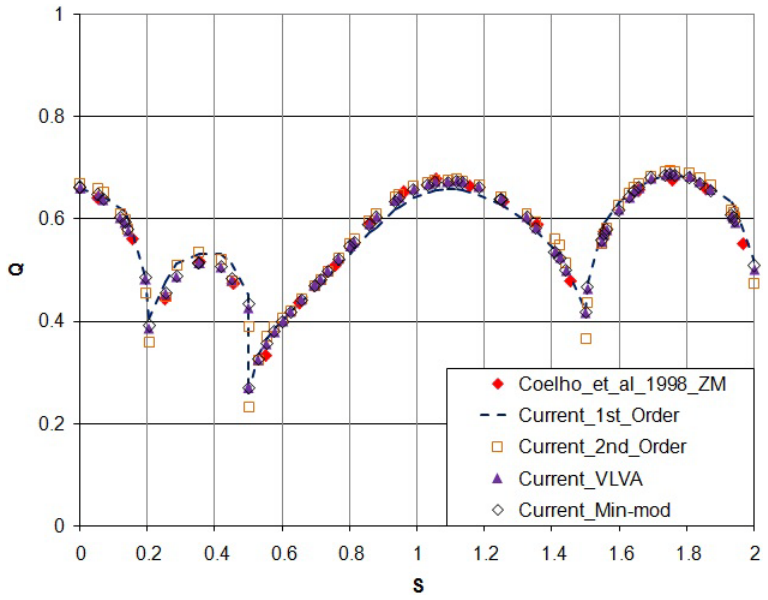

Figure 19: Distributions of incident radiative heat flux along the ABCD line for the initial mesh with black enclosures.

In order to assure that the differentiation between the first and the second order spatial schemes originates indeed from the upgrading of the spatial resolution, a twice dense mesh was utilized, including 46,198 nodes, 58,624 tetrahedrons and 66,024 prisms, in which all the available schemes were implemented again. A slight improvement is noticed for the first and the simple second order scheme in the region between 0.2m and 0.4m, while for the schemes enhanced with limiters no difference can be identified (Figure 20).

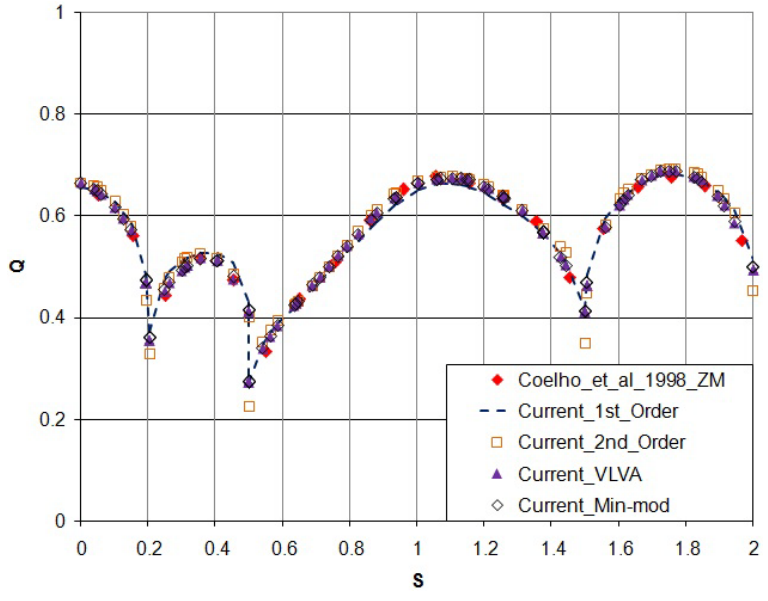

Figure 20: Distributions of incident radiative heat flux along the ABCD line for the twice dense mesh with black enclosures.

An additional case was encountered with grey walls instead, considering an emissivity value equal to 0.8 for the walls and 0.6 for the baffles. In Figure 21 the corresponding distributions of incident radiative heat flux are presented, all closely compared to the ones computed with Z-M (Zone-Method) of Coelho et al. [40].

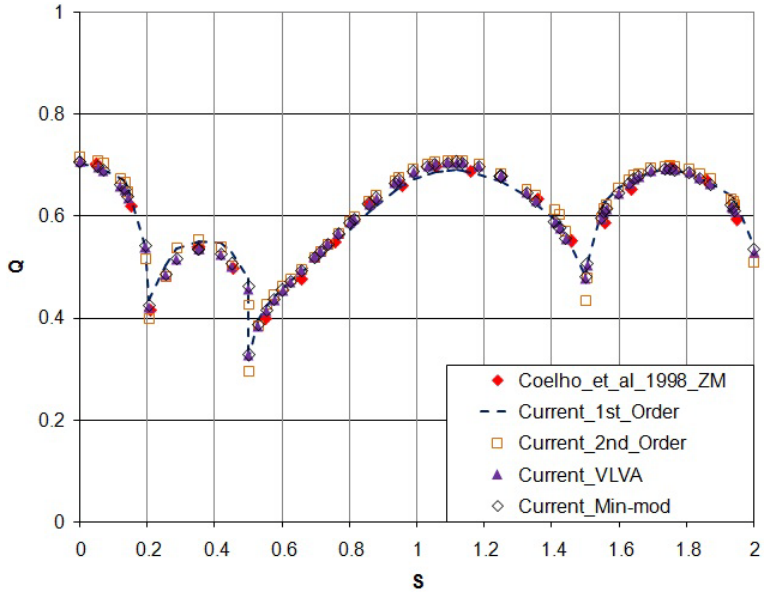

Figure 21: Distributions of incident radiative heat flux along the ABCD line for the initial mesh, with gray enclosures.

6 CONCLUSIONS

In this study an algorithm using a second order scheme in space and time, along with the h-refinement technique and a precomputational pixelation method is developed to improve the accuracy of radiative heat transfer predictions in three-dimensional unstructured hybrid grids. Though the previous methods are well established methodologies in CFD, they are rarely implemented in the prediction of radiative heat transfer. As the numerical results reveal, the higher order spatial schemes, especially these jointed with slope limiters, mitigate sufficiently the false scattering, derived by the finite spatial discretization. Their employment along with a second order in time method for the iterative solution of the time dependent RTE prevents the development of oscillations during the simulation, which is usually met when the second order spatial scheme is coupled to the standard iterative solution of the RTE [11, 12]. In addition, h-refinement technique revealed its potential to improve the accuracy of the algorithm during the progress of the solution, when the utilized mesh isn't fine enough, avoiding the generation of a finer mesh from the beginning. Although their employment increases the computational and memory requirements, they can be assumed relatively negligible, considering the accuracy improvement succeeded in coarse grids.

ACKNOWLEDGEMENTS

Part of this work was funded by ELXIS Engineering Consultants S.A. and the EUROSTARS Project (E!5292) "Structural and aerodynamic design of TUNnels under Fire Emergency Conditions".

REFERENCES

[1] G.D. Raithby and E.H. Chui, A finite-volume method for predicting a radiant heat transfer in enclosures with participating media, *J. Heat Transfer*, **112**, 415-423, 1990.

[2] G. Kim, S. Kim and Y. Kim, Parallelized unstructured-grid finite volume method for modeling radiative heat transfer, *J. Mech. Sci.Tech.*, **19**, 1006-1017, 2005.

[3] E.H. Chui, G.D. Raithby and P.M.J. Hughes, Prediction of radiative transfer in cylindrical enclosures with the finite volume method, *J. Thermophys. Heat Transfer*, **6**, 605-611, 1992.

[4] J.Y. Murthy and S.R. Mathur, Radiative heat transfer in axisymmetric geometries using an unstructured finite-volume method, *Num. Heat Transfer B*, **33**, 397-416, 1998.

[5] S.W. Baek and M.Y. Kim, Modification of the discrete ordinates method in an axisymmetric cylindrical geometry, *Num. Heat Transfer B*, **31**, 313-326, 1998.

[6] M.Y. Kim, S.W. Baek and J.H. Park, Unstructured finite-volume method for radiative heat transfer in a complex two-dimensional geometry with obstacles, *Num. Heat Transfer B*, **39**, 617-635, 2001.

[7] M.B. Salah, F. Askri, K. Slimi and S.B. Nasrallah, Numerical resolution of the radiative transfer equation in a cylindrical enclosure with the finite volume method, *Int. J. Heat Mass Transfer*, **47**, 2501-2509, 2004.

[8] P. Talukdar, M. Steven, F.V. Issendorff and D. Trimis, Finite volume method in 3-D curvilinear coordinates with multiblocking procedure for radiative transport problems, *Int. J. Heat Mass Transfer*, **48**, 4657-4666, 2005.

[9] M.Y. Kim, S.W. Baek and S.I. Park, Evaluation of the finite-volume solutions of radiative heat transfer in a complex two-dimensional enclosure with unstructured polygonal meshes, *Num. Heat Transfer B*, **54**, 116-137, 2008.

[10] C. Kim, M.Y. Kim, M.Y. Yu and S.C. Mishra, Unstructured polygonal finite-volume solutions of radiative heat transfer in a complex axisymmetric enclosure, *Num. Heat Transfer B*, **57**, 227-239, 2010.

[11] G.N. Lygidakis and I.K. Nikolos, Using the finite-volume method and hybrid unstructured meshes to compute radiative heat transfer in 3-D geometries, *Num. Heat Transfer B*, **62**, 289-314, 2012.

[12] G.N. Lygidakis and I.K. Nikolos, A parallelized node-centered finite volume method for computing radiative heat transfer on 3D unstructured hybrid grids, *11th Bien. Conf. Engin. Sys. Des. Anal. (ASME-ESDA 2012),* Nantes, France, 2 - 4 July, 2012.

[13] G.D. Raithby, Discussion of the finite volume method for radiation, and its application using 3D unstructured meshes, *Num. Heat Transfer B*, **35**, 389-405, 1999.

[14] J.C. Chai, H.S. Lee and S.H. Patankar, Ray effect and false scattering in the discrete ordinates method, *Num. Heat Transfer B*, **24**, 373-389, 1993.

[15] P.J. Coelho, Bounded skew high-order resolution schemes for the discrete ordinates method, *J. Computational Physics*, **175**, 412-437, 2002.

[16] R. Capdevila, C.D. Perez-Segarra and A. Oliva, Development and comparison of different spatial numerical schemes for the radiative transfer equation resolution using three-dimensional unstructured meshes, *J. Quant. Spectrosc. Radiat. Transfe*r, **111**, 264-273, 2010.

[17] J.Blazek, *Computational fluid dynamics: principles and applications*, Kidlington, Elsevier Science, 2001.

[18] G.D. Van Albada, B. Van Leer and W.W. Roberts, A comparative study of computational methods in cosmic gas dynamics, *J. Astrophys. Astron.,* **108**, 46-84, 1982.

[19] P.K. Sweby, High resolution schemes using flux limiters for hyperbolic conservation laws, *SIAM J. for Numer. Anal.,* **21**, 995-1011, 1984.

[20] B. Hunter and Z. Guo, Comparison of the discrete-ordinates method and the finite-volume method for steady-state and ultrafast radiative transfer analysis in cylindrical coordinates, *Num. Heat Transfer B*, **59**, 339-359, 2011.

[21] Z.M. Tan and P.F. Hsu, Transient radiative heat transfer in three-dimensional homogenous and non homogenous participating media, *J. Quant. Spectrosc. Radiat. Transfe*r, **73**, 181-194, 2002.

[22] J.C. Chai, One-dimensional transient radiation heat transfer modeling using a finite-volume method, *Num. Heat Transfer B*, **44**, 187-208, 2003.

[23] M.H. Lallemand, Etude de schemas Runge-Kutta a 4 pas pour la resolution multigrille des equations d' Euler 2D, *Raport de Recherche, INRIA*, 1988.

[24] Y. Kallinderis, A 3-D finite volume method for the Navier Stokes equations with adaptive hybrid grids, *Applied Numerical Mathematics,* **20**, 387-406, 1996.

[25] A. Khawaja, T. Minyard and Y. Kallinderis, Adaptive hybrid grid methods, *Computer Methods in Applied Mechanics and Engineering,* **180**, 1231-1245, 2000.

[26] C. Kavouklis and Y. Kallinderis, Parallel adaptation of general three-dimensional hybrid meshes, *J. Computational Physics*, **229**, 3454-3473, 2010.

[27] R. Lohner, Finite element methods in CFD: grid generation, adaptivity and parallelization, AGARD-R-787, *Proc. of the AGARD-FDP-VKI special course at VKI*, Rhode-Saint-Genese, 2-6 March, 1992.

[28] G.N. Lygidakis and I.K. Nikolos, An unstructured node-centered finite volume method for computing 3D viscous compressible flows on hybrid grids, *7th Int. Cong. on Comp. Mech. (7th GRACM)*, Athens, Greece, 30 June - 2 July, 2011.

[29] H. Jimbo, R. Liming and T. Heping, Effect of anisotropic scattering on radiative heat transfer in two-dimensional rectangular media, *J. Quant. Spectrosc. Radiat. Transfe*r, **78**, 151-161, 2003.

[30] G.C. Clark, C.M. Chu and S.W. Churchill, Angular distribution coefficients for radiation scattered by a spherical particle, *J. Opt. Soc. of Am.*, **47**, 81-84, 1957.

[31] J.E. Hunt, The Generation of angular distribution coefficients for radiation scattered by a spherical particle, *J. Quant. Spectrosc. Radiat. Transfe*r, **10**, 857-864, 1970.

[32] J. Liu, H.M. Shang and Y.S. Chen, Development of an unstructured radiation model applicable for two-dimensional planar, axisymmetric, and three-dimensional geometries, *J. Quant. Spectrosc. Radiat. Transfe*r, **66**, 17-33, 2000.

[33] A. Fiterman, R. Ben-Zvi and A. Kribus, DOTS: Pseudo-time-stepping solution of the discrete ordinate equations, *Num. Heat Transfer B*, **35**, 163-183, 1999.

[34] T.J. Barth, Aspects of unstructured grids and finite-volume solvers for the Euler and Navier-Stokes equations, AGARD-R-787, *Proc. of the AGARD-FDP-VKI special course at VKI*, Rhode-Saint-Genese, 2-6 March, 1992.

[35] B. Smith, P. Bjorstad and W. Gropp, *Domain Decomposition. Parallel multilevel methods for elliptic partial differential equations*, Cambridge University Press, Cambridge, 1996.

[36] METIS: http://glaros.dtc.umn.edu/gkhome/views/metis.

[37] S. Lanteri, Parallel solutions of compressible flows using overlapping and nonoverlapping mesh partitioning strategies, *Parallel Comput.*, **22**, 943–968, 1996.

[38] T.K. Kim and H. Lee, Effect of anisotropic scattering on radiative heat transfer in two-dimensional rectangular enclosures, *Int. J. Heat Mass Transfer*, **31**, 1711-1721, 1988.

[39] J.Y. Murthy and S.R. Mathur, A finite volume method for radiative heat transfer using unstructured meshes, *36th Aerospace Sciences Meeting & Exhibit (AIAA98-0860),* Reno, NV, 12 - 15 January, 1998.

[40] P.J. Coelho, J.M. Goncalves and M.G. M.G. Carvalho, Modelling of radiative heat transfer in enclosures with obstacles, *Int. J. Heat Mass Transfer*, **41**, 745-756, 1998.